

Data-driven Super-Resolution of Flood Inundation Maps using Synthetic Simulations

Akshay Aravamudan, Zimeena Rasheed, Xi Zhang, Kira E. Scarpignato,
Efthymios I. Nikolopoulos, Witold F. Krajewski, and Georgios C. Anagnostopoulos *Senior Member, IEEE*

Abstract—The frequency of extreme flood events is increasing throughout the world. Daily, high-resolution (30m) Flood Inundation Maps (FIMs) observed from space play a key role in informing mitigation and preparedness efforts to counter these extreme events. However, the temporal frequency of publicly available high-resolution FIMs, *e.g.*, from Landsat, is at the order of two weeks thus limiting the effective monitoring of flood inundation dynamics. Conversely, global, low-resolution (~300m) Water Fraction Maps (WFMs) are publicly available from NOAA VIIRS daily. Motivated by the recent successes of deep learning methods for single image super-resolution, we explore the effectiveness and limitations of similar data-driven approaches to downscaling low-resolution WFMs to high-resolution FIMs. To overcome the scarcity of high-resolution FIMs, we train our models with high-quality synthetic data obtained through physics-based simulations. We evaluate our models on real-world data from flood events in the state of Iowa. The study indicates that data-driven approaches exhibit superior reconstruction accuracy over non-data-driven alternatives and that the use of synthetic data is a viable proxy for training purposes. Additionally, we show that our trained models can exhibit superior zero-shot performance when transferred to regions with hydroclimatological similarity to the U.S. Midwest.

Index Terms—flood inundation maps, super-resolution, water fraction maps, machine learning

I. INTRODUCTION

CLIMATE change has exposed an increasing population to flood risks, especially over the last decade[1]. Floods, even with low return periods, tend to cause damage that may take years to recover and these efforts tend to disfavor low-income, racial and ethnic minorities due to a difficulty in accessing federal resources as well as time taken for congressional appropriation [2]. With an average recurrence interval of at least once in 200 years, the Bellavue, TN flood event in 2021 tallied to over 100 million USD in costs and claimed at least 20 lives [3]. Similarly, with a return period of once in 400 years, large-scale flooding across Europe in 2021 added to the list of record-breaking floods in the region claiming approximately 240 lives and over 25 billion USD in damages[4].

Studying the dynamics of flood inundation can better equip stakeholders to mitigate the damage caused by such floods

A. Aravamudan, X. Zhang, K. E. Scarpignato and G. C. Anagnostopoulos are with the Computer and Engineering Sciences Department at Florida Institute of Technology
Z. Rasheed and E. I. Nikolopoulos are with the Civil and Environmental Engineering at Rutgers University
W. F. Krajewski is with the Civil and Environmental Engineering at University of Iowa

Manuscript received XX XX, XXXX; revised XX XX, 20XX.

[5]. While Water Fraction Maps (WFMs) – which indicate the fraction of flood inundated pixels in the representative region – are obtainable on a daily basis, their resolution may prove too coarse to be useful for tasks such as the study of inundation dynamics. On the other hand, fine-resolution Flood Inundation Maps (FIMs), while useful for such tasks, are not available on a daily basis. Hence, the need arises to have more frequent, high-resolution FIMs which are binary images that indicate whether a specific location is inundated with water. This will aid in the study of inundation dynamics whose use-cases range from improved hydrological models, pre-flood mitigation strategies, underwriting flood insurance, property evaluation, and formulating evacuation plans to name a few.

Recent progress in satellite-based remote-sensing algorithms have provided stakeholders with flood related observations at global scales with existing products such as the NASA/NOAA Visible Infrared Imaging Radiometer Suite (VIIRS)¹, NASA Moderate Resolution Imaging Spectroradiometer (MODIS)² and NASA/USGS Landsat³. However, the coarse spatial resolution of MODIS (250m) and the long revisit times of Landsat (~16 days) hinder the analysis of the spatiotemporal dynamics of flood hazard at a range of spatial scales (from small creeks to big rivers) and terrains (from natural floodplains to urban settlements). WFMs, are available via existing satellite products (NOAA VIIRS and NASA MODIS) at a daily temporal frequency and at the cost of reduced image resolution. Naturally, using these WFMs to produce high quality FIMs at higher spatio-temporal resolution can prove advantageous to studying flood dynamics at a finer scales.

In this work, we investigate the task of downscaling low-resolution WFMs (300m) to high-resolution FIMs (30m) with computational approaches inspired by the successes of deep learning models in the field of super-resolution imaging [6]. We explore the utility of three state-of-the-art deep learning models –namely Residual Channel Attention Network (RCAN), Residual Dense Network (RDN) and Efficient Super Resolution Transformer (ESRT). The circumstances of our problem setting introduce a training data scarcity problem due to the following reasons: (i) we can record high resolution ground truth FIMs from Landsat only once every 16 days, (ii) the probability of observing a flood event during these satellite

¹<https://www.nesdis.noaa.gov/current-satellite-missions/currently-flying/joint-polar-satellite-system/visible-infrared-imaging>

²<https://modis.gsfc.nasa.gov>

³<https://landsat.gsfc.nasa.gov/>

visits further reduces our opportunities to collect data and (iii) flood events are relatively rare. These constraints makes it extremely hard to compile high quality datasets for a region of interest, especially for the data-driven models we seek to train. To alleviate this problem, we opted to use synthetic (SYN) data generated by physics-based simulations wherein the resolution can be controlled, admittedly at a significantly higher computational cost. With this solution, we postulate that SYN data can function as a viable proxy for real-world (RW) data.

We conducted experiments on four regions – namely, Iowa, Western Europe, Red-River and Ghana – and show that:

- SYN data are a viable proxy to existing scarce RW flood inundation data.
- Among the models we’ve trained using the SYN Iowa data, there are performance benefits, when evaluated on RW Iowa data.
- Our trained ML models are transferable with zero-shot performance benefits when applied to hydroclimatologically similar regions (according the Köppen classification scheme [7]) such as Western Europe and fails to show significant benefit when evaluated in hydroclimatologically dissimilar regions such as Ghana and Red-River.

The rest of the paper is organized as follows. Section II details some of the existing works and their limitations as we pave the path towards our proposed models in Section IV. Section III describes the datasets and pre-processing steps that we employed for this study. We describe our experimental setting in Section V, followed by a discussion of the results in Section VI. The GitHub repository containing the code and data has also been published⁴.

II. RELATED WORK

Within the realm of geophysical sciences, super-resolution/downscaling is a challenge that scientists continue to tackle. There have been several works involved in downscaling applications such as river mapping [8], coastal risk assessment [9], estimating soil moisture from remotely sensed images [10] and downscaling of satellite based precipitation estimates [11] to name a few. We direct the reader to [12] for a comprehensive review of satellite based downscaling applications and methods. Pertaining to our objective of downscaling WFMs, we can draw comparisons with several existing works. In what follows, we provide a brief review of functionally adjacent works to contrast the novelty of our proposed model and its role in addressing gaps in literature.

When it comes to downscaling WFM, several works use statistical downscaling techniques. These works downscale images by using statistical techniques that utilize relationships between neighboring water fraction pixels. For instance, [13] treat the super-resolution task as a sub-pixel mapping problem, wherein the input fraction of inundated pixels must be exactly mapped to the output patch of inundated pixels. [14] improved upon these approaches by including a spectral term to fully

utilize spectral information from multi spectral remote sensing image band. [15] on the other hand also include a spectral correlation term to reduce the influence of linear and non-linear imaging conditions. All of these approaches are applied to water fraction obtained via spectral unmixing [16] and are designed to work with multi spectral information from MODIS. However, we develop our model with the intention to be used with water fractions directly derived from the output of satellites. One such example is NOAA/VIIRS whose water fraction extraction method is described in [17]. [18] presented a work wherein WFM at 375-m flood products from VIIRS were downscaled 30-m flood event and depth products by expressing the inundation mechanism as a function of the Digital Elevation Map (DEM)-based water area and the VIIRS water area.

On the other hand, the non-linear nature of the mapping task lends itself to the use of neural networks. Several models have been adapted from traditional single image digital super-resolution in computer vision literature [19]. Existing deep learning models in single image super-resolution are primarily dominated by Convolutional Neural Network (CNN) based models. Specifically, there has been an upward trend in residual learning models. RDNs [20] introduced residual dense blocks that employed a contiguous memory mechanism that aimed to overcome the inability of very deep CNNs to make full use of hierarchical features. RCANs [21] introduced an attention mechanism to exploit the inter-channel dependencies in the intermediate feature transformations. There have also been some works that aim to produce more lightweight CNN-based architectures [22], [23]. Since the introduction of the vision transformer [24] that utilized the self-attention mechanism – originally used for modeling text sequences – by feeding a sequence 2D sub-image extracted from the original image. Using this approach [25] developed a light-weight and efficient transformer based approach for single image super-resolution.

For the task of super-resolution of WFMs, we discuss some works whose methodology is similar to ours even though they differ in their problem setting. [8] presented a cascaded spectral spatial model for super-resolution of MODIS imagery with a scaling factor 10. Their architecture consists of two stages; first multi-spectral MODIS imagery is converted into a low-resolution WFM via spectral unmixing by passing it through a deep stacked residual CNN. The second stage involved the super-resolution mapping of these WFMs using a nested multi-level CNN model. Similar to our work, the input fraction images are obtained with zero errors which may not be reflective of reality since there tends to be sensor noise, the spatial distribution of whom cannot be easily estimated. We also note that none of these works directly tackle flood inundation since they’ve been trained with river map data during non-flood circumstance and *ergo* do not face a data scarcity problem as we do. [26] used a deep CNN for land mapping that consists of several classes such as building, low vegetation, background and trees. [27] similarly employ a CNN based model for downscaling of summer monsoon rainfall data over the Indian subcontinent. Their proposed Super-Resolution Convolutional Neural Network (SRCNN) has a downscaling factor of 4. [28] on the other hand, proposed a super-resolution

⁴<https://github.com/aaravamudan2014/SIDDIS>

mapping technique using Generative Adversarial Networks (GANs). They first generate high resolution fractional images, somewhat analogous to our WFM, and are then mapped to categorical land cover maps involving forest, urban, agriculture and water classes. [29] interestingly approach lake area super-resolution for Landsat and MODIS data as an unsupervised problem using a CNN and are able to extend to other scaling factors. [30] performed flood inundation mapping using Synthetic Aperture Radar (SAR) data obtained from Sentinel-1. They showed that DEM-based features helped to improve SAR-based predictions for quadratic discriminant analysis, support vector machines and k-nearest neighbor classifiers. While almost all of the aforementioned works can be adapted to our task. We stand out in the following ways (i) We focus on downscaling of WFMs directly, *i.e.*, we do not focus on the algorithm to compute the WFM from multi-channel satellite data and (ii) We focus on producing high resolution maps only for instances of flood inundation. The latter point produces a data scarcity issue which we seek to remedy with synthetic data.

III. DATA DESCRIPTION

A. Synthetic & Real-world Data

We used synthetic flood inundation data for the entire state of Iowa, provided by the Iowa Flood Center [31]. Synthetic flood maps were derived from steady-state simulations for design flows that correspond to a range of probability of exceedance (USGS, Bulletin 17) using one-dimensional open-channel flow model from the Hydrologic Engineering Center's River Analysis System (HEC-RAS) 5. The river channel geometric properties, such as slopes and cross sections, were derived from airborne LiDAR based one-meter DEM data. For more details of the flood inundation mapping procedures see [32]. These simulated FIMs counter the issue of securing an already-limited availability of real-world FIMs, and proves advantageous to deep learning models that leverage increased data input for the super resolution task.

The test dataset contained a withheld sample of the synthetic FIMs but, more importantly, we prepared RW, satellite-based data derived from Landsat-8 output. These RW samples allow us to evaluate the generalizability of our trained downscaling model. Our targeted test regions utilizing RW data were located both in and out of Iowa (the region used for training). This motivates our research question about how effective deep learning models can transfer across other hydroclimatological regions. Landsat-8-based FIMs were generated for two sites within Iowa: at Cedar River and Des Moines River. Outside of the training region, FIMs were prepared for the flood events occurring in Red River in the North of the USA, the Nasia river in Ghana and Western Europe. Table I contains the chosen abbreviations for each of these study regions along with the period when the flooding occurred. Figure 1 shows the chosen locations for this paper.

Generating WFMs: For both SYN and RW data, we produce the WFMs by finding the ratio of inundated pixels in every 10x10 patch of pixels in the high resolution FIM. For RW data, we can obtain coarse resolution RW WFMs from

existing satellite products such as NOAA/VIIRS and the equivalent high resolution FIM from other satellite observations such as Landsat. However, in reality the differences between the two in terms of, primarily, timing of observations and secondly the algorithms applied for water detection, introduce discrepancies between coarse and high-res scenes that would contaminate the evaluation of high-res FIMs produced by the super-resolution algorithms. To avoid this source of error and focus the evaluation only on the effectiveness of the algorithms examined, we elected to create the coarse resolution RW WFMs by aggregating the high-res FIMs from Landsat. This means that, by construction, the number of inundated pixels in the high resolution FIM is exactly obeyed. However this may not be reflective of reality since real world WFM may be inundated with sensor noise, along with the errors induced by the algorithm that generate these WFMs.

B. Pre-processing coarse- and high-resolution imagery

RW FIMs were generated using multi-spectral images of Landsat-8 for the aforementioned flood events. Cloud free scenes were selected and the Spectral Water Index (SWI), defined as $SWI \triangleq \frac{Blue-NIR}{Red+Green+Blue}$, was used for water detection, where NIR refers to the Near Infrared band. An SWI threshold value was selected for each flood event after quantitative comparison of the histograms between non-flooded and flooded scenes and was applied for the binary classification of pixels to flooded and non-flooded. The resulting FIMs were also visually compared against visible Landsat-8 images for consistency. The coarse resolution WFMs that provide pixel values recorded as water fractions in the range $[0, 1]$ were prepared when 30m high-resolution FIMs having frame sizes 100×100 were down-sampled by a scale factor of 10. Resultantly, coarse resolution FIMs were 300m/pixel, 10×10 images. The high resolution FIMs reported binary pixel values of 0 or 1 indicating no-flood and flood cells, respectively.

IV. METHODOLOGY

We denote a low-resolution WFM by $\mathbf{X} \in [0, 1]^{L \times L}$. Our objective will be to learn a map $\mathbf{M} : [0, 1]^{L \times L} \rightarrow \{0, 1\}^{H \times H}$ that will downscale \mathbf{X} to a high-resolution FIM $\hat{\mathbf{Y}} \in \{0, 1\}^{H \times H}$, where $H = fL$ and $f > 1$ is a scale factor, so that $\hat{\mathbf{Y}}$ recovers the (true) FIM \mathbf{Y} that is associated to \mathbf{X} . In our work, we use $f = 10$ to replicate the spatial resolution produced by existing high resolution satellite products. In order to learn $\mathbf{M}(\cdot)$, we assume that each model we consider aims to learn the conditional joint probability $p(\mathbf{Y}|\mathbf{X})$. Furthermore, for simplicity, we will assume that the entries of \mathbf{Y} (FIM pixel intensities) are mutually independent, when conditioned on the entries of \mathbf{X} (WFM pixel intensities), *i.e.*, $p(\mathbf{Y}|\mathbf{X}) = \prod_{i,j} p(Y_{i,j}|\mathbf{X})$. Finally, assuming that the model accurately estimates the probabilities $p(Y_{i,j} = 1|\mathbf{X})$ via $S_{i,j}(\mathbf{X}) \in [0, 1]$, the FIM pixel intensities are reconstructed as $\hat{Y}_{i,j} = 1$, if $S_{i,j}(\mathbf{X}) \geq 0.5$ and 0, if otherwise. In what follows, we present the neural-based architectures we have chosen to implement the map $\mathbf{M}(\cdot)$ for this downscaling task.

Table I: Chosen regions of this study. We group the datasets into Iowa and External datasets.

Training FIMs [Location]	Validation/Test FIMs [Location]	Time period of flood.	Abbrev.	Samples
[Iowa]	Synthetic [Iowa]	N/A	SYN-IA	2,610
	Landsat-8 [Cedar River, Iowa]	Sep 2016	RW-IA(CR)	583
	Landsat-8 [Des Moines River, Iowa]	March 2019	RW-IA(DM)	531
	Landsat-8 [Europe]	July 2021	RW-EU	311
[External]	Landsat-8 [Red River, North America]	April 2020	RW-RR	582
	Landsat-8 [Nasia River, Ghana]	Sep 2007	RW-GH	31



Figure 1: Chosen regions for this study. Iowa is the region where the model was trained over, whereas all the other regions comprise of climatically similar (Europe) and dissimilar (Ghana, Red River) regions.

A. Model Architectures

There have been a variety of works that use deep learning techniques to learn highly complex mappings between the low- and high-resolution images. Note that, in our data, most of regions are not inundated with floods. This means that the output patch that corresponds to a water fraction of zero will be all zeros (no inundation). The same applies to fully inundated pixels. Therefore, once mapped to a higher resolution, we simply need to learn the residual map between the WFM and FIM. A residual connection from the input to the output therefore plays an important role in such architectures. This connection, in essence, crudely down-scales a WFM to a FIM and the network learns a modification to this mapping that performs better at down-scaling. This naturally leads us to the path of residual learning. Residual learning aims to learn the residual, or difference, between the output and input images [33]. Residual learning is mainly motivated by the following reasons (i) an unexpected training performance degradation, when networks grow deeper and, hence, should overfit and perform better and (ii) training becomes less prone to exploding or vanishing gradients.

In order to be able to train deep architectures we will rely on residual learning, which offer the aforementioned benefits. More specifically, we use RDNs [20] and RCANs [21] (see [6] for a comparative analysis). Apart from this, we also consider an efficient transformer based architecture called ESRT [25] that has been shown to be a strong competitor of late. A

common thread among all of these architectures is a shallow feature extraction layer and a final dense fusion layer. The final stage incorporates global residual learning and feature fusion to produce feature vectors, which are then passed through a transposed convolution layer – see [34] – in order to bring it to a size of 100×100 before being passed through a few more convolution layers to produce the high resolution FIM. In the following subsections, we briefly describe the individual architectures.

1) *RDN*: RDNs [20] combine the use of residual learning and of densely connected convolutional blocks: each such block consists of a number of convolutional layers, whose inputs consist of the outputs of all previous layers (via skip connections) within the same block; these inputs are regarded as hierarchical features. Finally, a skip connection routes the input of such blocks to their outputs in order to implement a type of local residual learning. RDNs employ global residual learning and consist of a long cascade of such blocks and a final upsampling stage that yields the down-scaled image. In our RDN architecture, we use 12 features in the convolutional layers, a kernel size of 3, 20 residual blocks and 20 layers per residual block.

2) *RCAN*: The RCAN was introduced in [21]. RCANs make use of channel attention, which aims to exploit the inter-dependencies between feature channels. This is done by first aggregating channel-wise features and applying a gating mechanism that learns non-linear relationships between

the feature channels. Following this, the features are passed through Residual-in-Residual (RIR) blocks, wherein residual learning is enforced. RIR blocks contain Residual Channel Attention Blocks (RCABs), which allows the network to focus on the important aspects of the low resolution features. In our model, we used 10 residual groups, each of which contains several residual blocks with short skip connection, 10 residual channel attention blocks, 64 features, kernel size of 3 and a reduction factor of 16.

3) *ESRT*: Transformers have shown to be quite effective in sequential tasks for natural language processing in comparison to convolutional neural networks [24]. The self-attention mechanism in transformers was applied to computer vision tasks in [35] by treating each image as a sequence of sub-images. While transformers typically feature an encoder and a decoder block when used for natural language processing tasks, for computer vision tasks they only feature an encoder to embed images into some feature space and then use another deep learning architecture for downstream tasks such as classification and super-resolution. [25] proposed the Efficient Super Resolution Transformer (ESRT), a low-complexity transformer architecture tailored to super-resolution tasks. In our usage of ESRT, we used 3 encoder layers with 32 features and kernel size of 3, each with a channel attention layer. The attention layer was a multi-scale local attention block consisting of 288 features.

B. Training

All of our data-driven, downscaling models were trained to minimize a penalized version of the average (over pixels) cross-entropy for each data pair (\mathbf{X}, \mathbf{Y})

$$L_{\text{PACE}}(\mathbf{X}, \mathbf{Y}) \triangleq L_{\text{ACE}}(\mathbf{Y}, \mathbf{S}(\mathbf{X})) + \eta P(\mathbf{X}, \mathbf{S}(\mathbf{X})) \quad (1)$$

where $\eta \geq 0$ is a penalty parameter and

$$L_{\text{ACE}}(\mathbf{Y}, \mathbf{S}(\mathbf{X})) \triangleq \frac{1}{H^2} \sum_{i,j} [Y_{i,j} \ln S_{i,j}(\mathbf{X}) + (1 - Y_{i,j}) \ln(1 - S_{i,j}(\mathbf{X}))] \quad (2)$$

$$P(\mathbf{X}, \mathbf{S}(\mathbf{X})) \triangleq \sum_{i,j} \left(X_{i,j} - \frac{1}{f^2} \sum_{k,l} S_{fi+k, fj+l}(\mathbf{X}) \right)^2 \quad (3)$$

where $i, j \in \{0, 1, \dots, L - 1\}$ and $k, l \in \{0, 1, \dots, f - 1\}$. The penalty term $P(\cdot, \cdot)$ quantifies the deviation between the fraction of inundated pixels in a $f \times f$ FIM patch vis-à-vis its corresponding WFM pixel. Using higher values of the penalty parameter η for training our downscaling models, significantly penalizes even modest deviations and, in essence, enforces the matching of water fractions between FIMs and WFMs. In our study, this was important as such matching occurred in our SYN data. Finally, let us point out that we treated η as a model hyper-parameter.

The weights of the neural network were optimized using Adam [36] with a decaying learning rate. The hyper-parameters along with their ranges in parentheses are as follows. The learning rate (10^{-5} to 10^{-4}), η (0 to 2000), layer dropout probability (10^{-3} to 20^{-2}), random seed (100

to 900 in multiples of 100). For the RDN, number of features (8 to 64 in multiples of 8), number of residual blocks (2 to 16 in multiples of 2), number of layers per block (2 to 32 in multiples of 2) and the kernel size was fixed to 3. For the RCAN, number of features (4 to 64 in multiples of 4), number of residual groups (10 to 40 in multiples of 5), number of residual channel attention blocks (20 to 50 in multiples of 5), reduction factor (16 to 64 in multiples of 4). For the ESRT, we used the hyper-parameters as available in the code for [25]. We used Optuna⁵ which in turn used the Tree-structured Parzen Estimator [37] to produce candidates for hyper-parameter search.

V. EXPERIMENTAL EVALUATION

A. Baseline Algorithms

We compared our neural-based downscaling models to two baseline methods, namely bicubic and Lanczos interpolation. Both of these methods are extensively used in common image processing tasks, including image downscaling. The former uses a polynomial kernel, while the later uses a product of cardinal sines to interpolate between WFM samples. The resulting image intensities are subsequently thresholded to yield a binary-valued FIM.

B. Metrics

All the downscaling models we consider employ an adjustable threshold $\theta \in [0, 1]$, based on which an array of pixel-on probabilities $S_{i,j}$ is thresholded to obtain a binary FIM. We will refer to the fraction of FIM pixels whose state (inundated vs. non-inundated) is correctly predicted, when using $\theta = 0.5$, as *accuracy*. Apart from this metric and due to the asymmetric importance of predicting inundation vs. predicting the lack of it at a locality, we also recorded the Receiver Operating Characteristic (ROC) curve for each model, which depicts the model's true positive rate (hit rate) as a function of the false positive rate (false alarm rate). These curves were obtained by varying the threshold θ between 0 and 1 to obtain predictions from the trained models and allow a stakeholder to establish an acceptable false alarm rate. Finally, due to the pronounced imbalance between the numbers of inundated and dry localities, we also report the models' Matthews Correlation Coefficient (MCC), which ranges in $[0, 1]$ and gauges how much more accurate a model is over always predicting that every locality is dry. An MCC of 0 indicates no improvement over a naïve model that always predicts no inundation for all pixels. Finally, we need to note that we only aggregate the results for pixels wherein the water fraction is between 0.25 and 0.85. This was done to exclude non-riverine regions and the areas in the middle of the river that contribute heavily to the aforementioned metrics due to their large proportion in FIMs. We also report the Prediction Intervals (PI) of the accuracies for each model. This was calculated using the Clopper-Pearson [38] prediction intervals for binomial proportion with a confidence level of 0.99.

⁵<https://optuna.readthedocs.io/en/stable/#>

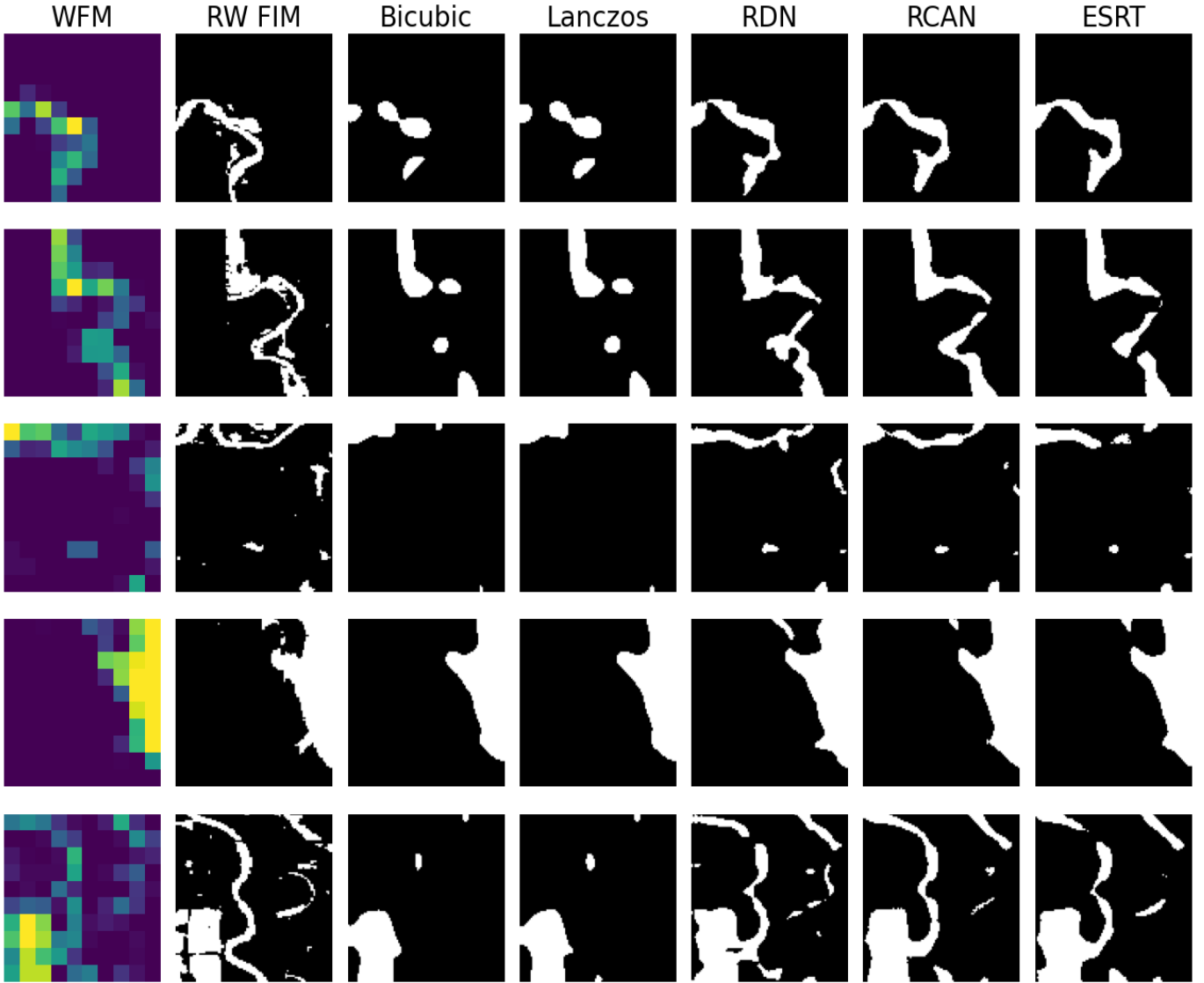


Figure 2: Sample outputs for the RW Iowa Des Moines region; *i.e.*, the region over which the model was trained.

Table II: Accuracies, along with their Prediction Intervals (PI) and Matthews Correlation Coefficient (MCC) of our models for Iowan Real-world (RW) and Synthetic (SYN) data. Real-world (RW) were obtained from Landsat-8 data, while synthetic (SYN) data were provided by the Iowa Flood Center. Note that we only present results for pixels where the water fraction in the WFM is in the interval (0.25, 0.85). Naïve model here represents outputs where all the pixels are predicted as non-inundated, *i.e.*, the majority class. Percentages depicted in bold signify the best performing model in each case.

Model	SYN-Iowa			RW-Iowa (CR)			RW-Iowa (DM)		
	accuracy (%)	accuracy PI (%)	MCC	accuracy(%)	accuracy PI (%)	MCC	accuracy(%)	accuracy PI (%)	MCC
Naïve	50.74	[50.66, 50.82]	0.0	49.83	[49.55, 50.10]	0.0	52.29	[52.02, 52.56]	0.0
bicubic	73.27	[73.20, 73.35]	0.475	69.96	[69.71, 70.21]	0.404	70.63	[70.38, 70.87]	0.418
Lanczos	73.72	[73.65, 73.79]	0.483	70.25	[70.00, 70.49]	0.409	70.89	[70.65, 71.14]	0.423
RDN	78.64	[78.57, 78.70]	0.574	70.65	[70.40, 70.90]	0.414	70.52	[70.28, 70.77]	0.410
RCAN	79.91	[79.85, 79.98]	0.599	72.69	[72.45, 72.93]	0.454	72.93	[72.69, 73.17]	0.457
ESRT	80.33	[80.27, 80.40]	0.607	73.31	[73.07, 73.55]	0.466	73.34	[73.10, 73.58]	0.465

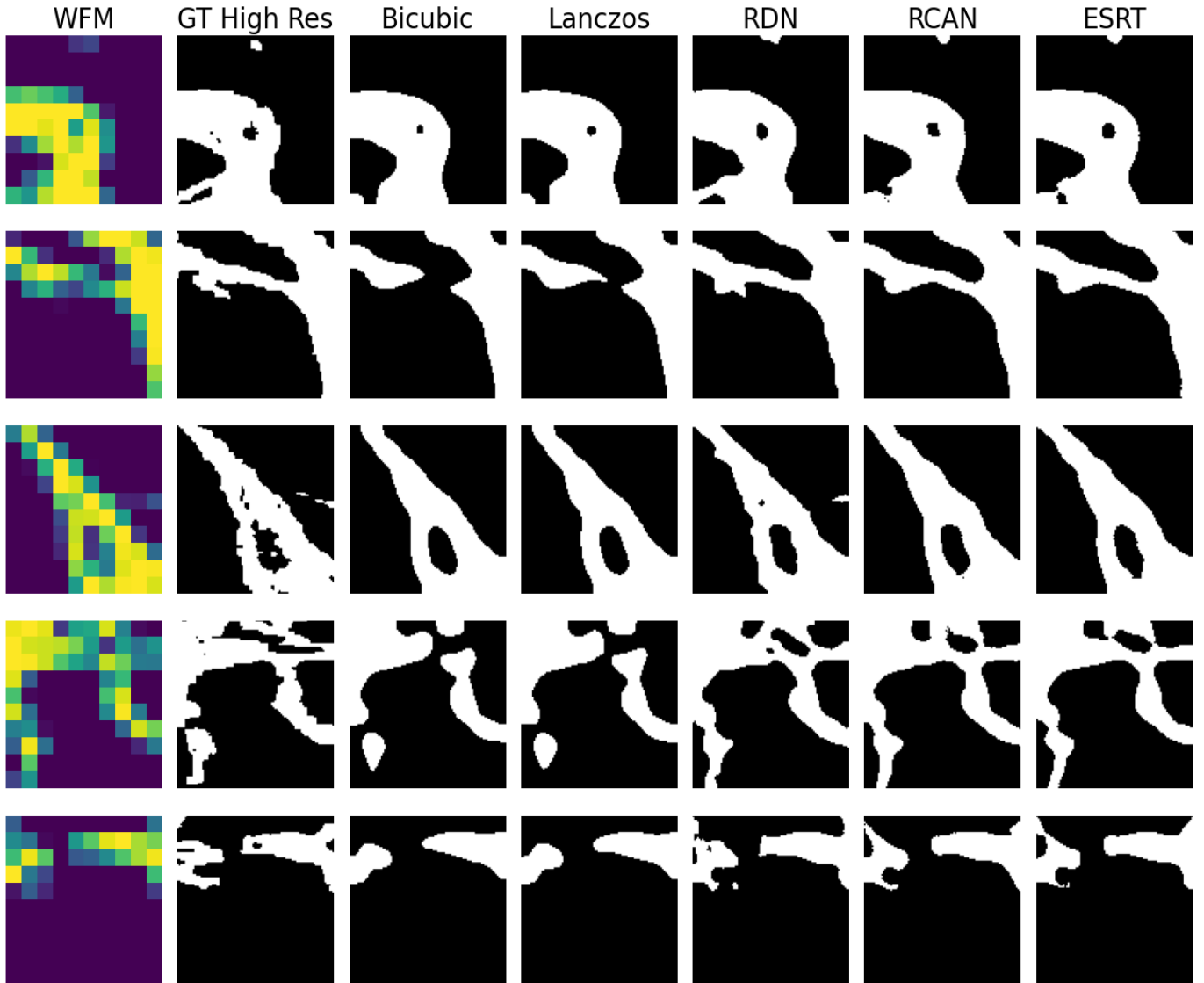


Figure 3: Sample outputs for the RW EU region; *i.e.*, external to the regions over which the model was trained.

Table III: Accuracies along with their Prediction Intervals (PI) and Matthews Correlation Coefficient (MCC) of our models for all external Real-world (RW) data. Real-world (RW) were obtained from Landsat-8 data. Note that we only present results for pixels where the water fraction in the WFM is in the interval (0.25, 0.85). Naïve model here represents outputs where all the pixels are predicted as non-inundated, *i.e.*, the majority class. Percentages depicted in bold signify the best performing model in each case.

Model	RW-EU			RW-GH			RW-RR		
	accuracy (%)	accuracy PI (%)	MCC	accuracy(%)	accuracy PI (%)	MCC	accuracy(%)	accuracy PI (%)	MCC
Naïve	47.03	[46.67, 47.39]	0.0	47.77	[47.08, 48.46]	0.0	40.86	[40.71, 41.01]	0.0
bicubic	77.77	[77.47, 78.07]	0.558	73.11	[72.50, 73.73]	0.463	71.39	[71.25, 71.52]	0.395
Lanczos	78.38	[78.09, 78.68]	0.570	73.50	[72.89, 74.11]	0.471	71.55	[71.42, 71.69]	0.399
RDN	80.97	[80.69, 81.25]	0.618	71.70	[71.07,72.32]	0.432	69.60	[69.46, 69.74]	0.361
RCAN	82.13	[81.86, 82.41]	0.641	73.97	[73.36, 74.57]	0.478	71.89	[71.76, 72.03]	0.4083
ESRT	83.27	[83.00, 83.54]	0.664	73.72	[73.11, 74.57]	0.474	72.32	[72.18, 72.45]	0.419

VI. RESULTS AND DISCUSSIONS

In this section, we aim to answer three main questions. First, we want to validate our hypothesis that SYN data is a viable proxy for RW data when training ML models for downscaling. Secondly, we seek to assess how much more skillful ML-

based downscaling is compared to classical, non-data-driven techniques, such as our baseline methods, *i.e.*, thresholded bicubic and Lanczos interpolation. Finally, we would like to appraise the extent to which data-driven models like ours are transferable (in terms of usefulness) to other regions without

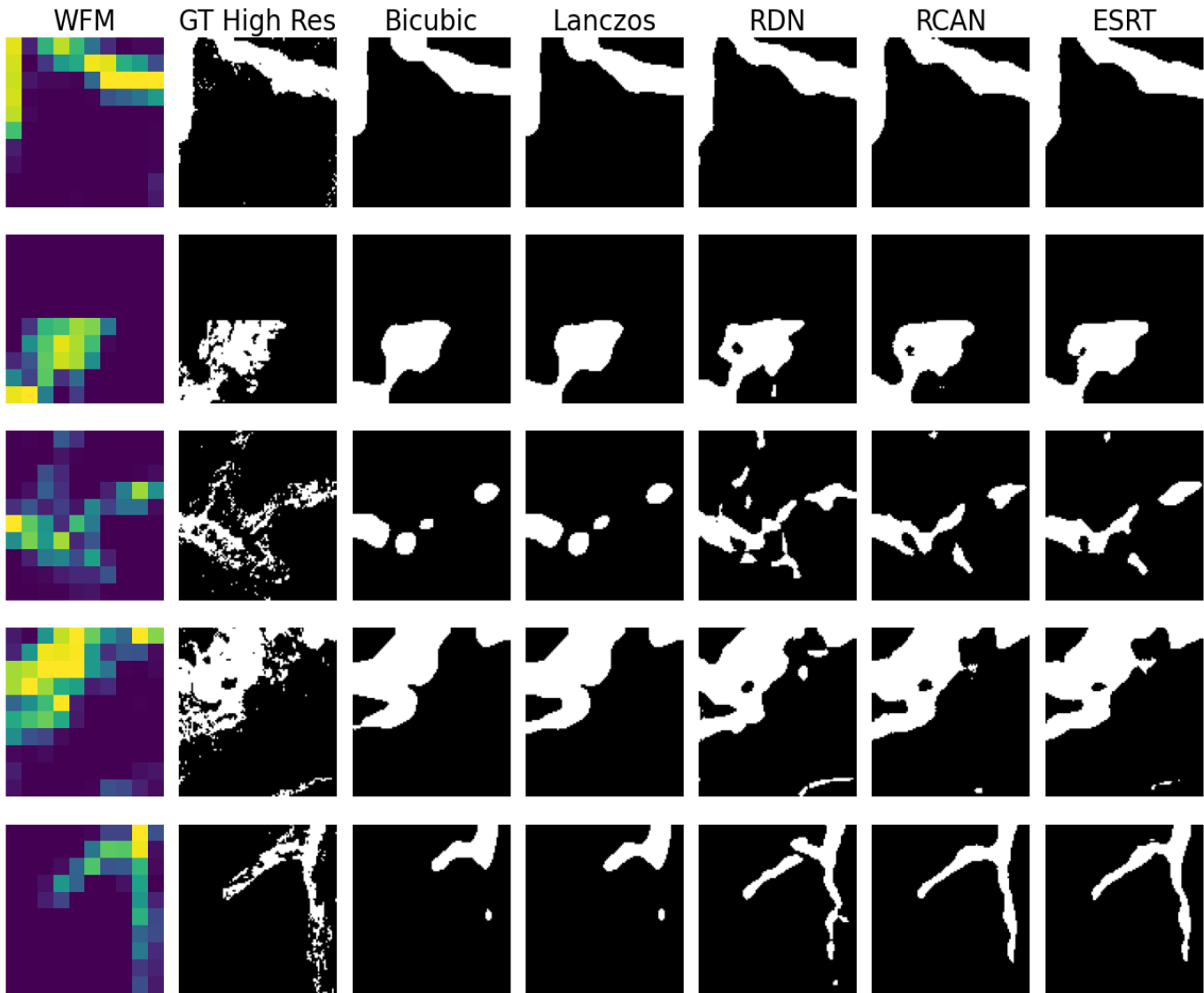


Figure 4: Sample outputs for the RW Ghana region; *i.e.*, external to the regions over which the model was trained.

major performance degradations. To assess the quality of the models, we conduct a multiple comparison test –namely the Holm-Bonferroni procedure [39] – that is designed to control the Family-Wise Error Rate (FWER). We notice that, with a FWER of 10^{-3} , all the differences in model performance are significant. The only exception to this trend was observed in RW-GH for whom the pairwise differences between RCAN and ESRT, Lanczos and Bicubic were not significant with the aforementioned FWER.

A. Potential of using SYN Data for RW downscaling

In order to evaluate the utility of synthetic data for training, we compare performances of our candidate models on both SYN and RW Iowa data whose results are presented in Table II. We notice that (i) For the Iowa datasets, there is a drop in performance of all the models when going from SYN to RW datasets, (ii) for the RW-IA (CR) as well as RW-IA (DM) datasets, both bicubic and Lanczos interpolation have accuracies and MCC up to 70.89% and 0.42 respectively

while the deep learning models have accuracies and MCC up to 73.34% and 0.46 respectively, (iii) There is a roughly 6% accuracy improvement for the SYN data for the deep learning models compared to the bicubic and lanczos models and this improvement drops to about 3% for RW data, (iv) the performance of all the models remain consistent across both RW-IA datasets and (v) in Figure 5, we observe that there is a high degree of overlap among the ROC curves for the data-driven models.

From (i) and (iv) we can conclude that SYN data is more intricate than RW data. This implies that the benefits yielded by training with SYN dataset, while significant, is not as prominent in the RW Iowa datasets. (i), (iii) and (v) implies that while SYN data is not an exact replacement for RW data, it provides a rather significant edge, which is all the more important when there is insufficient RW for training. From (ii) we can conclude that the three proposed data driven models outperform classical super-resolution techniques such as bicubic and lanczos, conclusion supported by the ROC curves in Figure 5 for whom the data-driven models, in

general, lie above the non-data-driven alternatives. Observation (iv) shows that for the climatically similar RW-Iowa(CR) and RW-Iowa(DM) regions, training on SYN Iowa data does indeed provide an edge.

B. Effectiveness of data-driven approaches

In order to evaluate the effectiveness of ML models in the downscaling task, we compare performances of our candidate models to Lanczos and bicubic interpolation methods by looking at figures of some sample predictions from Iowa (Figure 2), performance comparison in the region of Iowa in Table II and the ROC curves in Figure 5 for RW data. We notice that (vi) For RW-IA (DM) samples, the deep learning models maintain a higher degree of spatial continuity in the predicted FIM, (vii) We observe that bicubic and Lanczos interpolation produces over-smoothed FIM reconstructions, while the plain RDN, RCAN and ESRT models are more detail-inclusive. Similar conclusions can be drawn upon inspecting the ROC curves in Figure 5 and (viii) For RW-IA (CR), the ML models show a performance improvement of 3.06% when comparing the best ML model and non-data-driven method and, while for RW-IA (DM) there is a performance improvement of 2.45%.

Figures 3 and 2 show the spatial disparity among the models whose details are often obscured in aggregated metrics such as accuracy. (vi) This implies that these data-driven models are better at recognizing an underlying stream network geometry than the classical methods. However, when it comes to narrow river streams, all the models struggle capturing the nuances of the FIM resultant from localized high elevation features such as small islands within rivers or man-made structures. (vii) shows a clear advantage of our data-driven approaches over the non-data-driven alternatives. (viii) indicates the benefits of the data-driven models when evaluated over Iowa.

C. Applicability of our models to external regions

To evaluate how transferable our models are, we draw conclusions from figures of the sample predictions from Western Europe (Figure 3) and Ghana (Figure 4) as well as the performance comparison in Table III. We notice that (ix) for Ghana all of the models fail to adequately inundate the pixels over separated areas on account of several disconnected regions of inundation in the chosen area, (x) the ML models outperform non-data driven methods for RW-EU, (xi) for the RW-EU dataset, there is an improvement of 4.89% when comparing the accuracy of the best data- and non-data-driven methods, (xii) For RW-RR and RW-GH, there is marginal improvement (up to 0.77% in accuracy) of the ML methods over the non-data driven methods and (xiii) For RW-EU, we notice that the ML models produce more connected streams over the non-data-driven models.

(x) and (xi) implies that the models are transferable when considering hydroclimatically similar regions since Iowa and the Meuse river in Europe lie within mid temperate zones. Similar to the observation (vi) for RW-IA (DM), (xiii) implies that the benefits of the ML model in identifying underlying network streams is also transferable to hydroclimatically similar regions. In contrast, (xii) and (ix) both imply that

the trained ML models struggle to generalize to RW-RR & RW-GH. We speculate that this may be due to the significant differences in geography and climate when compared to Iowa.

Our study directly implies that good quality synthetic data can be useful surrogates for downscaling low-resolution WFMs to high-resolution FIMs in regions, where such data are hard to come by, even when downscaling by a factor of 10. We noticed that such models were readily transferable to climatically similar regions as the region of training. However, Such derived ML models did not feature significantly different transferability when evaluated over hydroclimatologically dissimilar regions, which we attribute to different flood inundation characteristics, primarily at finer scales. A possible avenue to circumvent such issues is to explore additional training approaches that fall under the general area of domain adaptation. Nevertheless, data-driven models are still advantageous (and, hence, preferable) over non-data-driven alternatives in transfer scenarios like the one we considered here.

VII. CONCLUSION

In this work we study a $10\times$ data-driven super-resolution framework for converting WFMs into high resolution FIMs. High resolution FIMs help in the study of flood inundation dynamics for a variety of applications, including real-time emergency response. We propose three candidate ML models to produce FIMs. We also embellished the classical binary cross entropy loss with a soft constraint to enforce a loose satisfaction of the fractions in the WFM. To circumvent data scarcity, we train our proposed ML models using HEC-RAS simulations over the region of Iowa as a stand-in for real world data. To determine the efficacy of our proposed downscaling models, we evaluate the model over five regions, three with hydroclimatical similarity to the training dataset – Des Moines in Iowa, Cedar River in Iowa and the Meuse river in Western Europe – and two dissimilar regions – Red River of the north and Nasia river in Ghana. Our results indicate that, for geomorphological and hydroclimatological similar regions, a model trained on synthetic data yields benefits over traditional interpolation techniques for downscaling. This suggests that such synthetic data can act as a stand-in for training such data-intensive ML models. When extending these models to other regions, we notice that the benefits of synthetic data are less evident. It appears that training separate models per topographically similar regions may be the only recourse.

Note that our study focuses solely on riverine flooding and does not address pluvial or coastal inundation, this is left to future work. Additionally, we expect that a meaningful incorporation of topographic features to the deep learning architecture such as DEMs – as done in [18] – can help improve the downscaling performance. While this work was evaluated on data from Landsat, this methodology can easily be extended to other satellite products. The combination of the proposed method applied to coarse resolution optical data available daily with high-res SAR-based FIMs from Sentinel observations offers a unique opportunity for global scale flood inundation monitoring at high-resolution.

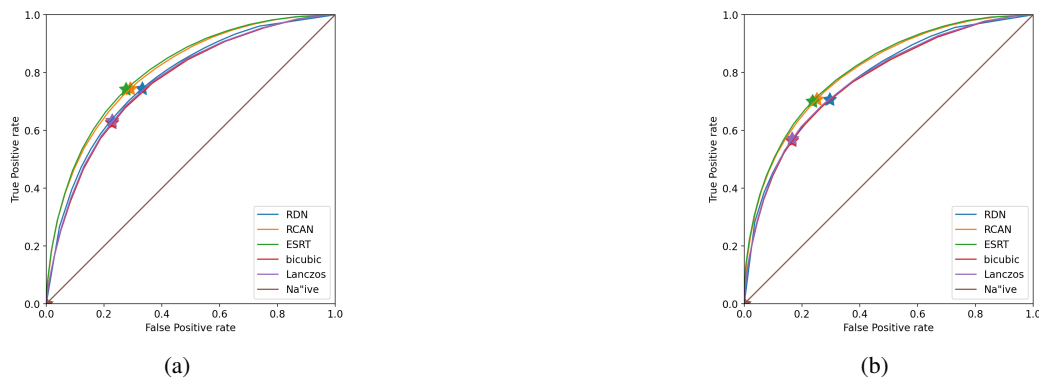


Figure 5: Receiver Operating Characteristic (ROC) curves for (a) RW-IA (CR) and (b) RW-IA (DM) dataset. Naïve model here represents a model whose output is solely a “no Flood” for all pixels. Star here represents the pixel-wise classifier with a threshold of 0.5.

ACKNOWLEDGMENT

The authors acknowledge partial support from an Institutional Research Incentive seed grant titled “*Satellite Imagery Downscaling via Deep Image Super-resolution*” and provided by the College of Engineering & Sciences of Florida Institute of Technology. Nikolopoulos acknowledges support from NOAA grant (NA200AR4600288) titled “*Accelerate the Exploitation of Satellite Observations to Improve Flooding and Inundation Monitoring and Forecasts*”. We would like to acknowledge high-performance computing support from Casper (doi:10.5065/D6RX99HX) provided by NCAR’s Computational and Information Systems Laboratory, sponsored by the National Science Foundation. The authors acknowledge Dr. Emanuel Storey for creating the Landsat based FIMs for the flood events in Red River, Iowa and Europe. The author also acknowledge the Iowa Flood Center for providing the outputs from the physics-based simulations.

REFERENCES

- [1] B. Tellman, J. A. Sullivan, C. Kuhn, A. J. Kettner, C. S. Doyle, G. R. Brakenridge, T. A. Erickson, and D. A. Slayback, “Satellite Imaging Reveals Increased Proportion of Population Exposed to Floods,” *Nature*, vol. 596, no. 7870, pp. 80–86, 2021. [Online]. Available: <https://doi.org/10.1038/s41586-021-03695-w>
- [2] B. Wilson, E. Tate, and C. Emrich, “Flood Recovery Outcomes and Disaster Assistance Barriers for Vulnerable Populations,” *Frontiers in Water*, vol. 3, p. 752307, 12 2021. [Online]. Available: <https://doi.org/10.3389/frwa.2021.752307>
- [3] NOAA, August 2021, Storm Events Database Entry for Damage Assessment. [Online]. Available: https://www.ncdc.noaa.gov/stormevents/listevents.jsp?eventType=%28C%29+Flash+Flood&eventType=%28Z%29+Flood&beginDate_mm=&beginDate_dd=21&beginDate_yyyy=2021&endDate_mm=08&endDate_dd=21&endDate_yyyy=2021&haifilter=0.00&tornfilter=0&windfilter=000&sort=DT&submitButton=Search&statefips=-999%2CALL
- [4] A. Post, July 2021, Article on Damage Assessment of European Floods. [Online]. Available: <https://www.actuarialpost.co.uk/article/european-floods-claim-240-lives-and-economic-loss-of-usd25bn-19920.htm>
- [5] B. Revilla-Romero, F. A. Hirpa, J. T.-d. Pozo, P. Salamon, R. Brakenridge, F. Pappenberger, and T. De Groeve, “On the Use of Global Flood Forecasts and Satellite-Derived Inundation Maps for Flood Monitoring in Data-Sparse Regions,” *Remote Sensing*, vol. 7, no. 11, pp. 15702–15728, 2015. [Online]. Available: <https://www.mdpi.com/2072-4292/7/11/15702>
- [6] Z. Wang, J. Chen, and S. C. H. Hoi, “Deep Learning for Image Super-Resolution: A Survey,” *IEEE Transactions on Pattern Analysis and Machine Intelligence*, vol. 43, pp. 3365–3387, 2021. [Online]. Available: <https://ieeexplore.ieee.org/stamp/stamp.jsp?arnumber=9044873>
- [7] D. Chen and H. W. Chen, “Using the Köppen classification to quantify climate variation and change: An example for 1901–2010,” *Environmental Development*, vol. 6, pp. 69–79, 2013. [Online]. Available: <https://www.sciencedirect.com/science/article/pii/S2211464513000328>
- [8] Z. Yin, F. Ling, X. Li, X. Cai, H. Chi, X. Li, L. Wang, Y. Zhang, and Y. Du, “A Cascaded Spectral–Spatial CNN Model for Super-Resolution River Mapping With MODIS Imagery,” *IEEE Transactions on Geoscience and Remote Sensing*, vol. 60, pp. 1–13, 2022. [Online]. Available: <https://ieeexplore.ieee.org/document/9623549>
- [9] C. A. Rucker, N. Tull, J. C. Dietrich, T. E. Langan, H. Mitasova, B. O. Blanton, J. G. Fleming, and R. A. Luettich, “Downscaling of Real-time Coastal Flooding Predictions for Decision Support,” *Natural Hazards*, vol. 107, no. 2, pp. 1341–1369, Jun 2021. [Online]. Available: <https://doi.org/10.1007/s11069-021-04634-8>
- [10] J. Peng, A. Loew, O. Merlin, and N. E. C. Verhoest, “A Review of Spatial Downscaling of Satellite Remotely Sensed Soil Moisture,” *Reviews of Geophysics*, vol. 55, no. 2, pp. 341–366, 2017. [Online]. Available: <https://agupubs.onlinelibrary.wiley.com/doi/abs/10.1002/2016RG000543>
- [11] S. C. Medrano, F. Satgé, J. Molina-Carpio, R. P. Zolá, and M.-P. Bonnet, “Downscaling Daily Satellite-Based Precipitation Estimates Using MODIS Cloud Optical and Microphysical Properties in Machine-Learning Models,” *Atmosphere*, vol. 14, no. 9, 2023. [Online]. Available: <https://www.mdpi.com/2073-4433/14/9/1349>
- [12] K. Karwowska and D. Wierzbicki, “Using Super-Resolution Algorithms for Small Satellite Imagery: A Systematic Review,” *IEEE Journal of Selected Topics in Applied Earth Observations and Remote Sensing*, vol. 15, pp. 3292–3312, 2022. [Online]. Available: <https://ieeexplore.ieee.org/stamp/stamp.jsp?arnumber=9757881>
- [13] L. Li, Y. Chen, X. Yu, R. Liu, and C. Huang, “Sub-pixel flood inundation mapping from multispectral remotely sensed images based on discrete particle swarm optimization,” *ISPRS Journal of Photogrammetry and Remote Sensing*, vol. 101, pp. 10–21, 2015. [Online]. Available: <https://www.sciencedirect.com/science/article/pii/S092427161400272X>
- [14] P. Wang, G. Zhang, and H. Leung, “Improving Super-Resolution Flood Inundation Mapping for Multispectral Remote Sensing Image by Supplying More Spectral Information,” *IEEE Geoscience and Remote Sensing Letters*, vol. 16, no. 5, pp. 771–775, 2019. [Online]. Available: <https://ieeexplore.ieee.org/document/8565995>
- [15] P. Wang, L. Wang, H. Leung, and G. Zhang, “Super-Resolution Mapping Based on Spatial–Spectral Correlation for Spectral Imagery,” *IEEE Transactions on Geoscience and Remote Sensing*, vol. 59, no. 3, pp. 2256–2268, 2021. [Online]. Available: <https://ieeexplore.ieee.org/stamp/stamp.jsp?arnumber=9130890>
- [16] L. Wang, D. Liu, Q. Wang, and Y. Wang, “Spectral Unmixing Model Based on Least Squares Support Vector Machine With Unmixing Residue Constraints,” *IEEE Geoscience and Remote Sensing Letters*, vol. 10, no. 6, pp. 1592–1596, 2013. [Online]. Available: <https://ieeexplore.ieee.org/document/6553106>
- [17] S. Li, D. Sun, Y. Yu, I. Csizsar, A. Stefanidis, and M. D. Goldberg, “A new Short-Wave Infrared (SWIR) Method for Quantitative Water Fraction Derivation and Evaluation with EOS/MODIS and Landsat/TM Data,” *IEEE Transactions on Geoscience and Remote*

- Sensing*, vol. 51, no. 3, pp. 1852–1862, 2013. [Online]. Available: <https://ieeexplore.ieee.org/document/6307841>
- [18] S. Li, D. Sun, M. D. Goldberg, S. Kalluri, B. Sjöberg, D. Lindsey, J. P. Hoffman, M. DeWeese, B. Connelly, P. Mckee, and K. Lander, “A Downscaling model for Derivation of 3-D Flood Products from VIIRS Imagery and SRTM/DEM,” *ISPRS Journal of Photogrammetry and Remote Sensing*, vol. 192, pp. 279–298, 2022. [Online]. Available: <https://www.sciencedirect.com/science/article/pii/S0924271622002349>
- [19] M. Sdraka, I. Papoutsis, B. Psomas, K. Vlachos, K. Ioannidis, K. Karantzas, I. Gialampoukidis, and S. Vrochidis, “Deep Learning for Downscaling Remote Sensing Images: Fusion and Super-Resolution,” *IEEE Geoscience and Remote Sensing Magazine*, vol. 10, no. 3, p. 202–255, 2022. [Online]. Available: <https://ieeexplore.ieee.org/document/9786720>
- [20] Y. Zhang, Y. Tian, Y. Kong, B. Zhong, and Y. Fu, “Residual Dense Network for Image Super-Resolution,” in *2018 IEEE/CVF Conference on Computer Vision and Pattern Recognition*, 2018, pp. 2472–2481. [Online]. Available: <https://ieeexplore.ieee.org/document/8578360>
- [21] Y. Zhang, K. Li, K. Li, L. Wang, B. Zhong, and Y. Fu, “Image Super-Resolution Using Very Deep Residual Channel Attention Networks,” *CoRR*, vol. abs/1807.02758, 2018. [Online]. Available: https://openaccess.thecvf.com/content_ECCV_2018/html/Yulun_Zhang_Image_Super-Resolution_Using_ECCV_2018_paper.html
- [22] Z. Hui, X. Gao, Y. Yang, and X. Wang, “Lightweight Image Super-Resolution with Information Multi-distillation Network,” in *Proceedings of the 27th ACM International Conference on Multimedia*, ser. MM ’19. New York, NY, USA: Association for Computing Machinery, 2019, p. 2024–2032. [Online]. Available: <https://doi.org/10.1145/3343031.3351084>
- [23] X. Luo, Y. Xie, Y. Zhang, Y. Qu, C. Li, and Y. Fu, “LatticeNet: Towards Lightweight Image Super-Resolution with Lattice Block,” in *Computer Vision – ECCV 2020*, A. Vedaldi, H. Bischof, T. Brox, and J.-M. Frahm, Eds. Cham: Springer International Publishing, 2020, pp. 272–289. [Online]. Available: https://www.ecva.net/papers/eccv_2020/papers_ECCV/papers/123670273.pdf
- [24] A. Vaswani, N. Shazeer, N. Parmar, J. Uszkoreit, L. Jones, A. N. Gomez, L. Kaiser, and I. Polosukhin, “Attention is All You Need,” in *Proceedings of the 31st International Conference on Neural Information Processing Systems*, ser. NIPS’17. Red Hook, NY, USA: Curran Associates Inc., 2017, p. 6000–6010. [Online]. Available: https://proceedings.neurips.cc/paper_files/paper/2017/file/3f5ee243547dce91fbd053c1c4a845aa-Paper.pdf
- [25] Z. Lu, J. Li, H. Liu, C. Huang, L. Zhang, and T. Zeng, “Transformer for Single Image Super-Resolution,” in *2022 IEEE/CVF Conference on Computer Vision and Pattern Recognition Workshops (CVPRW)*. Los Alamitos, CA, USA: IEEE Computer Society, jun 2022, pp. 456–465. [Online]. Available: <https://doi.ieeecomputersociety.org/10.1109/CVPRW56347.2022.00061>
- [26] Y. Jia, Y. Ge, Y. Chen, S. Li, G. B. M. Heuvelink, and F. Ling, “Super-Resolution Land Cover Mapping Based on the Convolutional Neural Network,” *Remote Sensing*, vol. 11, no. 15, 2019. [Online]. Available: <https://doi.org/10.3390/rs11151815>
- [27] B. Kumar, R. Chattopadhyay, M. Singh, N. Chaudhari, K. Kodari, and A. Barve, “Deep Learning–based Downscaling of Summer Monsoon Rainfall Data over Indian Region,” *Theoretical and Applied Climatology*, vol. 143, no. 3, pp. 1145–1156, 2021. [Online]. Available: <https://doi.org/10.1007/s00704-020-03489-6>
- [28] C. Shang, X. Li, G. M. Foody, Y. Du, and F. Ling, “Superresolution Land Cover Mapping Using a Generative Adversarial Network,” *IEEE Geoscience and Remote Sensing Letters*, vol. 19, pp. 1–5, 2022. [Online]. Available: <https://ieeexplore.ieee.org/document/9195742>
- [29] M. Qin, L. Hu, Z. Du, Y. Gao, L. Qin, F. Zhang, and R. Liu, “Achieving Higher Resolution Lake Area from Remote Sensing Images Through an Unsupervised Deep Learning Super-Resolution Method,” *Remote Sensing*, vol. 12, no. 12, 2020. [Online]. Available: <https://www.mdpi.com/2072-4292/12/12/1937>
- [30] F. Aristizabal, J. Judge, and A. Monsivais-Huerta, “High-Resolution Inundation Mapping for Heterogeneous Land Covers with Synthetic Aperture Radar and Terrain Data,” *Remote Sensing*, vol. 12, no. 6, 2020. [Online]. Available: <https://www.mdpi.com/2072-4292/12/6/900>
- [31] W. F. Krajewski, D. Ceynar, I. Demir, R. Goska, A. Kruger, C. Langel, R. Mantilla, J. Niemeier, F. Quintero, B.-C. Seo, S. J. Small, L. J. Weber, and N. C. Young, “Real-Time Flood Forecasting and Information System for the State of Iowa,” *Bulletin of the American Meteorological Society*, vol. 98, no. 3, pp. 539 – 554, 2017. [Online]. Available: <https://journals.ametsoc.org/view/journals/bams/98/3/bams-d-15-00243.1.xml>
- [32] D. Gilles, N. Young, H. Schroeder, J. Piotrowski, and Y.-J. Chang, “Inundation mapping initiatives of the iowa flood center: Statewide coverage and detailed urban flooding analysis,” *Water*, vol. 4, no. 1, pp. 85–106, 2012. [Online]. Available: <https://www.mdpi.com/2073-4441/4/1/85>
- [33] K. He, X. Zhang, S. Ren, and J. Sun, “Deep Residual Learning for Image Recognition,” in *2016 IEEE Conference on Computer Vision and Pattern Recognition (CVPR)*, 2016, pp. 770–778. [Online]. Available: <https://ieeexplore.ieee.org/stamp/stamp.jsp?arnumber=7780459>
- [34] W. Shi, J. Caballero, F. Huszar, J. Totz, A. P. Aitken, R. Bishop, D. Rueckert, and Z. Wang, “Real-Time Single Image and Video Super-Resolution Using an Efficient Sub-Pixel Convolutional Neural Network,” in *2016 IEEE Conference on Computer Vision and Pattern Recognition (CVPR)*. Los Alamitos, CA, USA: IEEE Computer Society, jun 2016, pp. 1874–1883. [Online]. Available: <https://doi.ieeecomputersociety.org/10.1109/CVPR.2016.207>
- [35] A. Dosovitskiy, L. Beyer, A. Kolesnikov, D. Weissenborn, X. Zhai, T. Unterthiner, M. Dehghani, M. Minderer, G. Heigold, S. Gelly, J. Uszkoreit, and N. Houlsby, “An Image is Worth 16x16 Words: Transformers for Image Recognition at Scale,” in *International Conference on Learning Representations*, 2021. [Online]. Available: <https://openreview.net/forum?id=YicbFdNTTy>
- [36] D. P. Kingma and J. Ba, “Adam: A Method for Stochastic Optimization,” in *International Conference on Learning Representations (ICLR) 2015*, 2015. [Online]. Available: <http://arxiv.org/abs/1412.6980>
- [37] J. Bergstra, R. Bardenet, Y. Bengio, and B. Kégl, “Algorithms for Hyper-Parameter Optimization,” in *Proceedings of the 24th International Conference on Neural Information Processing Systems*, ser. NIPS’11. Red Hook, NY, USA: Curran Associates Inc., 2011, p. 2546–2554. [Online]. Available: https://proceedings.neurips.cc/paper_files/paper/2011/file/86e8f7ab32cfd12577bc2619bc635690-Paper.pdf
- [38] C. J. Clopper and E. S. Pearson, “The Use of Confidence or Fiducial Limits Illustrated in the Case of the Binomial,” *Biometrika*, vol. 26, no. 4, pp. 404–413, 12 1934. [Online]. Available: <https://doi.org/10.1093/biomet/26.4.404>
- [39] S. Holm, “A Simple Sequentially Rejective Multiple Test Procedure,” *Scandinavian Journal of Statistics*, vol. 6, no. 2, pp. 65–70, 1979. [Online]. Available: <http://www.jstor.org/stable/4615733>

Akshay Aravamudan is a PhD student at the Florida Institute of Technology. His research areas of interest include machine learning, stochastic point processes for the study of information diffusion and influence characterization in social media, machine learning for hydrology and machine learning on the edge. Before joining FIT’s Center for Advanced Data Analytics & Systems (CADAS), he obtained his M.S. in Computer Engineering at the Florida Institute of Technology.

Zimeena Rasheed is a PhD student at Rutgers University, New Brunswick. She graduated with a M.S. in Civil Engineering from Florida Institute of Technology in 2020. Her research broadly includes the study of stream flows, their prediction for anticipation of floods as well as satellite-based flood inundation.

Xi Zhang is a PhD student at the Florida Institute of Technology. Her research interests include probabilistic modeling, statistical methods, ML/AI with applications in social media, cyber-security and the earth sciences. She received her M.S. in Electrical Engineering at Florida Institute of Technology, and she is currently a member of FIT’s Center for Advanced Data Analytics & Systems (CADAS).

Kira E. Scarpignato is expected to graduate with a B.S in Biomedical Engineering and a minor in Biology in May 2024 from Florida Institute of Technology. Her current research is focused on cardiovascular tissue engineering.

Efthymios I. Nikolopoulos is an Associate Professor of Civil & Environmental Engineering at Rutgers University, New Brunswick. He received his Engineering Diploma from the Technical University of Crete, Greece, his M.Sc. degree from the University of Iowa, and his Ph.D. degree from the University of Connecticut, U.S. He has also worked as a postdoc at the University of Padova, Italy. His expertise is in the modeling and monitoring of hydrometeorological and hydrologic extremes (extreme precipitation, floods, droughts, debris flows). His main research goal is to improve the understanding and predictability of hydrologic extremes and develop methods to mitigate their impacts.

Witold F. Krajewski received his Ph.D. from Warsaw University of Technology in 1980. He is the Rose & Joseph Summers Chair in Water Resources Engineering and Professor in Civil and Environmental Engineering at the University of Iowa. He serves as Director of the Iowa Flood Center, an entity funded by the State of Iowa in the United States and housed at the University of Iowa. His research interests include all aspects of flood forecasting. He is a Fellow of the American Meteorological Society (AMS), the American Geophysical Union (AGU), and a member of the U.S. National Academy of Engineering.

Georgios C. Anagnostopoulos is an Associate Professor of Electrical & Computer Engineering at the Florida Institute of Technology in Melbourne, Florida. He received his Engineering Diploma from the University of Patras in 1994 and his M.Sc. and Ph.D. degrees in Electrical Engineering from the University of Central Florida in 1997 and 2001 respectively. His areas of expertise are machine learning, modeling and optimization. He is a senior member of the IEEE.